


## Article

# Investigation on Ti-6Al-4V Microstructure Evolution in Selective Laser Melting

Ling Ding, Zhonggang Sun, Zulei Liang, Feng Li, Guanglong Xu  and Hui Chang \*

Tech Institute for Advanced Materials & College of Materials Science and Engineering, Nanjing Tech University, Nanjing 210009, China; dingling2013@njtech.edu.cn (L.D.); sunzgg@njtech.edu.cn (Z.S.); zuleiliang@163.com (Z.L.); fli@njtech.edu.cn (F.L.); guanglongxu@njtech.edu.cn (G.X.)

\* Correspondence: ch2006@njtech.edu.cn; Tel.: +86-138-1391-6521

Received: 17 October 2019; Accepted: 21 November 2019; Published: 27 November 2019



**Abstract:** Selective laser melting (SLM) is an advanced additive manufacturing technique that can produce complex and accurate metal samples. Since the process performs local high heat input during a very short interaction time, the physical parameters in the solidification are difficult to measure experimentally. In this work, the microstructure evolution of Ti-6Al-4V alloy in additive manufacturing was studied. With the increase of scanning speed, the cooling rate and the temperature gradient of molten pool position increased, which was attributed to the gradual decrease of energy density. The phase-field simulation resulted in the overall microstructure morphology of columnar crystals owing to the very large temperature gradient and cooling rate obtained from the temperature field. Microsegregation was observed during dendritic formation, and the solute was enriched in the liquid phase near the dendritic tip and between the dendritic arms due to the lower equilibrium distribution coefficient. The scanning speed had an effect on the dendrite spacing.

**Keywords:** SLM; simulation; microstructure; phase field

## 1. Introduction

Additive manufacturing technology has broken through the traditional material reduction manufacturing method, which relies on multiple processes combined in manufacturing. Based on the computer-aided design (CAD) and the integrated system of robots, the additive manufacturing can quickly and precisely manufacture parts with arbitrary complex shapes, thus realizing the real free manufacturing [1,2]. Nowadays, additive manufacturing is gaining more and more attention due to such advantages over traditional manufacturing as easier creation of complex geometries, optimized material usage, and cost savings in expensive tools [3,4].

Selective laser melting (SLM) is one of the new additive manufacturing techniques that emerged in the late 1980s and 1990s. Selective laser melting (SLM) forming technology is a technology based on the principle of additive manufacturing, which enables the manufacture of parts from bottom to top through layer-by-layer stacking of materials. The process requires a CAD model to be built on a computer, and then a layer of ultrafine titanium alloy powder with a thickness of 20 to 100  $\mu\text{m}$  laid on the powder bed. The metallurgical bonds are formed between the layers by the selective laser melting without adding an adhesive, which results in a high density of the parts with lower surface roughness. Due to the high precision, SLM is often used in the manufacture of titanium alloys.

Microstructure is a key factor affecting material properties, and the process of additive manufacturing is at the heart of its final characteristics. Tensile strength and ultimate tensile strength are highly related to the distribution and spacing of the dendrite arms [5,6] and the microsegregation has a strong influence on the distribution of dendrites. Razavi et al. discussed the fatigue properties of Ti-6Al-4V produced by SLM, which also reflects some relations with microstructure [7,8]. Lore Thijs et al. [9–12] studied

the influence of the scanning parameters and scanning strategy on the microstructure of Ti-6Al-4V processed by SLM. However, the process of nucleation and growth cannot be directly observed due to the complexity of the metallurgical process. At present, the method of simulation is in common use. Yang et al.'s research [13–17] concentrated on the finite element model for additive manufacturing, and the temperature field distribution of the additive manufacturing process was obtained, while macroscopic temperature field data were not introduced into the microstructure simulation, and there was a lack of description of the phase transition process. Gong et al. [18–20] studied the microstructure evolution of EBAM Ti-6Al-4V during solidification, while the microstructure simulation of Ti-6Al-4V processed by SLM was unattended. Through the combination of macroscopic finite element simulation and microscopic phase field simulation, this paper attempts to bring the influence of macroscopic parameters into the microstructure.

## 2. Model Description

In this paper, the most widely used titanium alloy Ti-6Al-4V was studied, as was shown in Figure 1, the macroscopic temperature field near the melt pool of the SLM sample was firstly simulated by finite element method to obtain the temperature gradient and cooling rate distribution. Then, the corresponding temperature field data was introduced into the microscopic phase field model to simulate the influence of process parameters on the microstructure. Finally, the experiments and the classical models were used to verify the results.

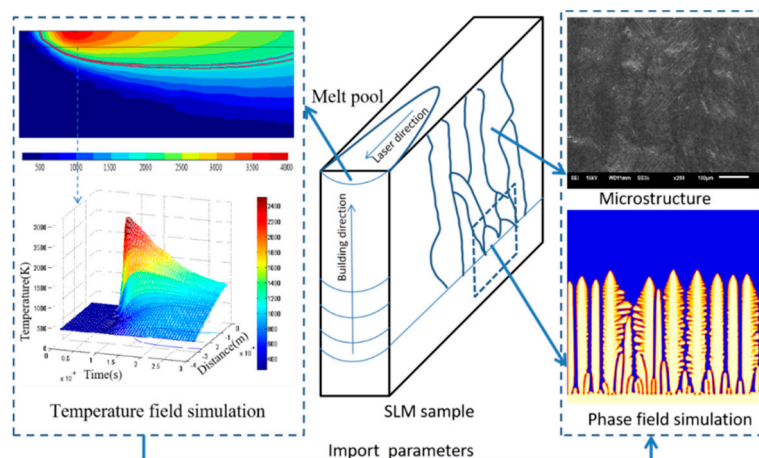


Figure 1. Research content.

### 2.1. Model of Rapid Solidification Finite Element

SLM is a heat-driven process, and temperature evolution behavior is the basis for studying the SLM process. Research on the temperature field of the SLM process can help researchers and engineers better predict the quality and performance of SLM samples. The numerical simulation software used in this paper is COMSOL 5.3 (COMSOL Inc, Stockholm, Sweden) In theory, COMSOL can couple any number of physical fields, and is often used in practical engineering problems in many fields such as electromagnetics, structural mechanics, acoustics, fluid flow, heat transfer, and chemical engineering [21].

In order to simplify the calculation in the finite element model, the powder layer and the powder bed are regarded as continuous media of equal density, and the material properties are considered to be related to the material properties of the solid and the porosity of the powder, which enables the powder material properties to be calculated from the physical material properties and the powder void fraction. There are a large number of voids inside the metal powder, and the material properties thereof are significantly different from the bulk metal. To simplify the calculation, the model treats metal powder and bulk metal as two materials. When the metal powder temperature is higher than the melting temperature, the metal powder is converted into a bulk metal material [22].

The temperature field geometry model is shown in Figure 2, which simulates the single-pass scanning process of a laser in a single layer of powder. The surface of the geometric model was set to a layer of powder with a length of 3610  $\mu\text{m}$ , width of 900  $\mu\text{m}$ , and thickness of 30  $\mu\text{m}$ . Below the powder layer is a substrate, which can also be set as a powder bed by changing the material properties, with a length of 3610  $\mu\text{m}$ , width of 900  $\mu\text{m}$ , and thickness of 90  $\mu\text{m}$ . In order to reduce the error of the calculation result and minimize the amount of calculation, the middle region of the powder layer (length of 2750  $\mu\text{m}$ , width of 500  $\mu\text{m}$ ) is divided into small meshes with the same size in a “mapping + scanning” manner. The length direction is equally divided into 100 parts, the width direction is equally divided into 20 parts, and the thickness direction is equally divided into 2 parts. Other areas are divided into tetrahedral meshes of different sizes in the form of “free tetrahedron + fine mesh”.

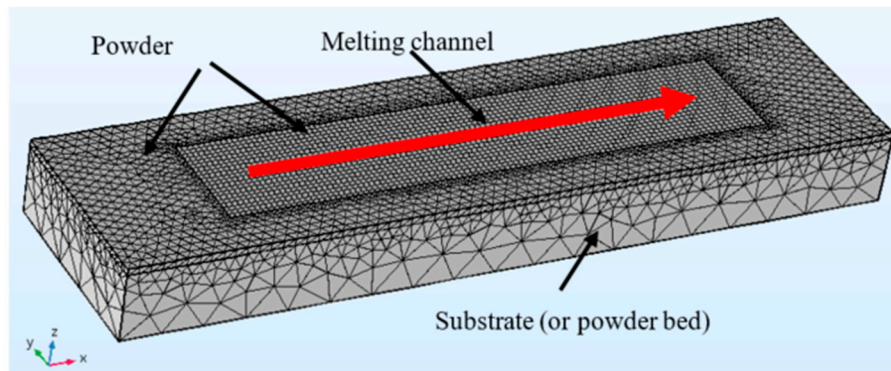


Figure 2. Diagram of thermal model and of coupled thermo-mechanical model.

The heat source in the model moves in the same way as the laser in the experiment; that is, single-track or zigzag point-by-point scanning. The equation of motion of the heat source is:

$$t_x = \text{mod}(t/2\Delta t_l) \quad (1)$$

$$x_t = \begin{cases} x_0 + \text{floor}(t_x/\Delta t_p) \cdot \Delta x & t_x \leq \Delta t_l \\ x_1 - \text{floor}(t_x/\Delta t_p) \cdot \Delta x & t_x \geq \Delta t_l \end{cases} \quad (2)$$

$$y_t = y_0 + \text{floor}(t/\Delta t_l) \cdot \Delta y \quad (3)$$

where the  $x$  direction is parallel to the melt channel (the direction of advancement of the heat source), and the  $y$  direction is the superposition direction of the melt channel.  $x_0$  and  $x_1$  are the starting point of  $x$  coordinate and the ending point of  $x$  coordinate of the melting channel, respectively,  $y_0$  is the starting point of  $y$  coordinate of the melting channel,  $x_t$  and  $y_t$  are the real-time coordinates of the heat source center, and  $t$  is the heat source moving time.  $\Delta t_p$  and  $\Delta t_l$  are, respectively, the heat source at one point. The dwell time and the residence time of the heat source on a melting channel,  $\text{mod}()$  is the remainder function,  $\text{floor}()$  is the rounding function, and  $\Delta x$  and  $\Delta y$  are the distance of the heat source scanning and the distance between the melt channels.

The temperature field simulation of SLM uses laser as the heat source to heat the latest powder layer. It is considered that the boundary temperature of the model away from the heat source remains unchanged, and the heat radiation on the surface of the material in the high temperature region and the thermal convection with the surrounding environment are also considered. Therefore, the SLM temperature field was simulated by selecting the fluid heat transfer (ht) physics field in COMSOL and setting the heat source, temperature, heat flux, and diffuse surface. In the SLM process, heat conduction is the main way of heat dissipation, following Fourier's law, i.e.,

$$\rho c \frac{\partial T}{\partial t} + \rho c u \cdot \Delta T + \nabla \cdot (-k \nabla T) = Q + Q_p \quad (4)$$

where  $\rho$  is the material density,  $c$  is the material heat capacity,  $u$  is the velocity vector of the molten metal (when the material state is metal powder or bulk metal,  $u$  is 0),  $k$  is the thermal conductivity of the material,  $Q$  is the external body heat source energy input, and  $Q_p$  is the heat generated or absorbed by the phase conversion. In this work, only the heat absorbed by the bulk metal melting and the heat generated when the molten metal solidifies are considered.

In this model, the starting point of the melting channel is the origin of the model; that is, the (0,0,0) point, the laser scans 31 points in the form of point scanning, the dot spacing is 55  $\mu\text{m}$ , and the laser stays 0.00005 s per point, which consumes a time of 0.00155 s. The material properties required for temperature field simulation include thermal conductivity, density, heat capacity, and laser heat source.

## 2.2. Model of Phase Field

The equilibrium partition coefficients of the Al and V elements calculated from the Thermo-Calc TTTi3 database are very close, and according to the study by Nastac et al. [23], treating the Al and V elements as a mixed element does not greatly affect the appearance of the phase field. Therefore, Al and V are regarded as a mixed element in this work. Referring to the research by Ramirez et al. [24] and Echebarria et al. [25], the following assumptions are made:

- (1) To simplify the model, Ti-6Al-4V is regarded as a binary alloy by treating the solute as a mixed AL-V element;
- (2) By default, the diffusion coefficient of the solute in the solid phase and the liquid phase does not change during the solidification temperature range;
- (3) The phase diagram data in the solidified temperature interval is unchanged by default;
- (4) The temperature field is applied in the form of a temperature gradient and a cooling rate, ignoring the latent heat of phase change.

The phase field model is built using micress 6.2 (ACCESS e.V. Aachen, Germany.) software with a grid size of  $500 \times 500$ , a cell resolution of 0.03  $\mu\text{m}$ , and a minimum time step of  $10^{-8}$  s. The initial conditions are considered to be 1 for the initial grain size, and the rectangular region at the bottom of the model is set to have a length of 15  $\mu\text{m}$  and a thickness of 0.15  $\mu\text{m}$ . Based on the principle of minimum free energy, the phase field equation of micress is used:

$$\dot{\phi}(\vec{x}, t) = \mu \left[ \sigma \left\{ \nabla^2 \phi - \frac{(1-\phi)(1-2\phi)\phi}{\eta^2} \right\} + \frac{1}{\eta} \Delta G \phi (1-\phi) \right] \quad (5)$$

where  $x$  is space,  $t$  is time,  $\Delta G$  is Gibbs free energy,  $\phi$  is the order parameter of phase field,  $\sigma$  is interfacial energy,  $\eta$  is interfacial thickness, and  $\mu$  is the interfacial mobility.

The boundary conditions are based on the symmetric boundary of the micress software. The phase field value of the boundary element is defined to be the same as the second adjacent element in the analog domain, thereby revealing that a plane of symmetry is crossing through the center of the outermost element of the region. This condition is similar to an isolation condition that moves half a unit. The interface thickness is 5 units. Referring to the research of Gong et al. [18–20], some physical parameters are obtained, as shown in Table 1.

**Table 1.** Partial Physical Parameters [18–20].

Physical Parameters	Ti-6Al-4V
Liquid diffusion coefficient $D_l$ ( $\text{cm}^2/\text{s}$ )	$9.5 \times 10^{-5}$
Solid diffusion coefficient $D_s$ ( $\text{cm}^2/\text{s}$ )	$5 \times 10^{-9}$
Gibbs Thomson coefficient $\Gamma$ (Km)	$1.88 \times 10^{-7}$
Distribution coefficient	0.5
Calculated temperature $T$ (K)	1890
Anisotropic strength $\eta$	0.1

### 3. Results and Discussions

#### 3.1. Finite Element Simulation of Temperature Field

The simulated temperature field is shown in Figure 3. The temperature at the boundary of the molten pool is set to 1850 K–1950 K. The vertical position to the center of the molten pool is selected to plot the temperature distribution with time. With the laser moving, the temperature near the molten pool first rises and then decreases; meanwhile, the heating rate is significantly bigger than the cooling rate. Along the direction from the powder bed to the base, the temperature gets lower and lower, and the cooling rate slows down gradually.

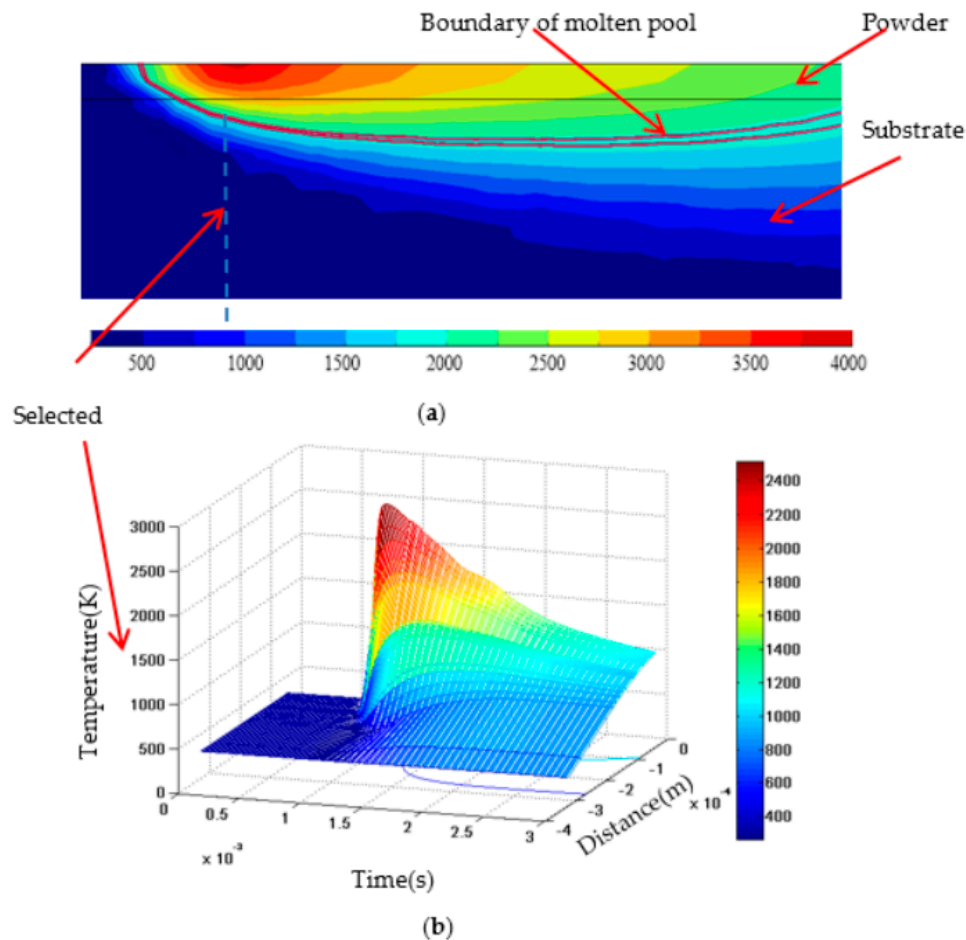


**Figure 3.** Diagrams of temperature field simulation results at a rate of 1000 mm/s, (a) temperature field distribution, (b) temperature change perpendicular to the center of the molten pool over time.

Since the temperature distribution and temperature gradient are affected by both time and position, and the variation range is large, the boundary of the powder bed and the substrate is the starting position of solidification. According to the boundary line of the molten pool boundary, the range shown in Figure 4 is selected. The solidification zone has a corresponding cooling rate according to the change of temperature in the range with time, and the initial temperature gradient within the range is the temperature gradient during solidification. As the laser moves to the left, the temperature distribution at the a-line position gradually evolves to the temperature distribution at the position of the b-line, and the solidification process is finished when the temperature at the intersection of the a-line and the molten pool boundary is cooled to the intersection of the b-line and the molten pool boundary.



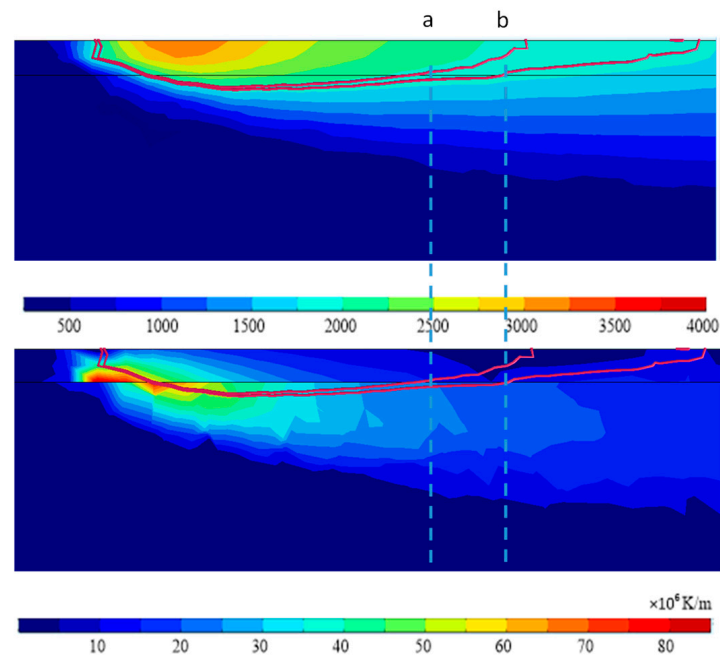


**Figure 4.** Diagram of the selection range of solidification area.

Select different scanning speeds and the resulting temperature distribution is shown in Figure 5. The temperature near the laser spot is the highest, close to 3500 K, while the temperature away from the spot is lower. Since the power of the laser does not change, the energy density near the laser spot will increase as the scanning speed decreases. As the scanning speed increases, the temperature peak near the laser spot gradually decreases. As shown in Figure 5a–f, the range of the molten pool boundary near the laser spot is narrower when the scanning speed is lower, while with increased scanning speed, the range of the molten pool boundary will gradually increase.

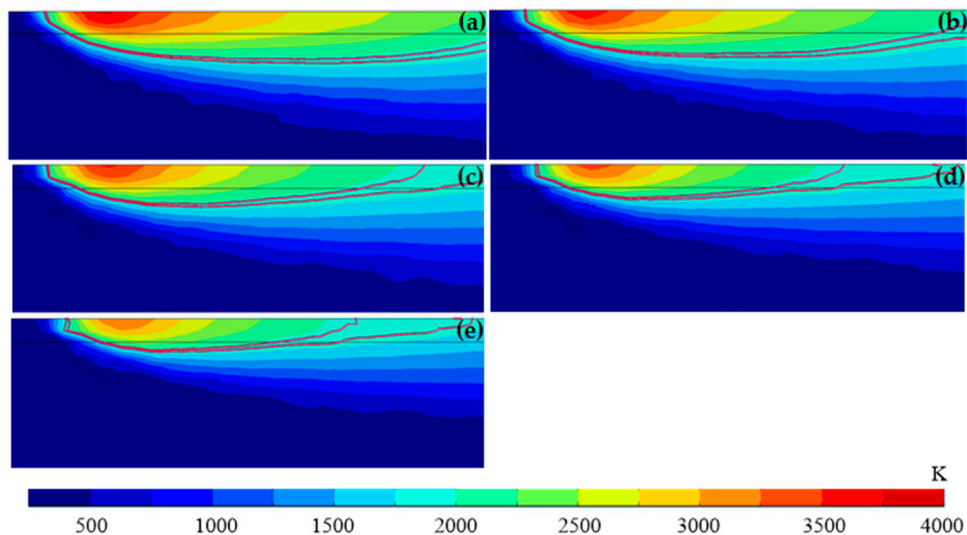


**Figure 5.** Effect of scanning speed on temperature field distribution, (a) 1000 mm/s, (b) 1100 mm/s, (c) 1200 mm/s, (d) 1400 mm/s, (e) 1600 mm/s.

The temperature gradient distribution at different scanning speeds are shown in Figure 6. The temperature gradient at the junction between the powder bed and the substrate is the highest, which is close to  $8 \times 10^5$  K/cm. The temperature gradient decreases overall as the distance becomes bigger. The overall variation of the temperature gradient near the molten pool is small, ranging from

$4 \times 10^4$  K/cm to  $2 \times 10^5$  K/cm, which is far lower than the temperature gradient near the laser spot. By comparing the temperature gradients at different scanning speeds, the scanning speed was noted to have a negligible influence on the peak of the temperature gradient, and the temperature gradient distribution near the spot is very close. However, by increasing the scanning speed, the energy density decreases, and the temperature changed area is noticed to be smaller.

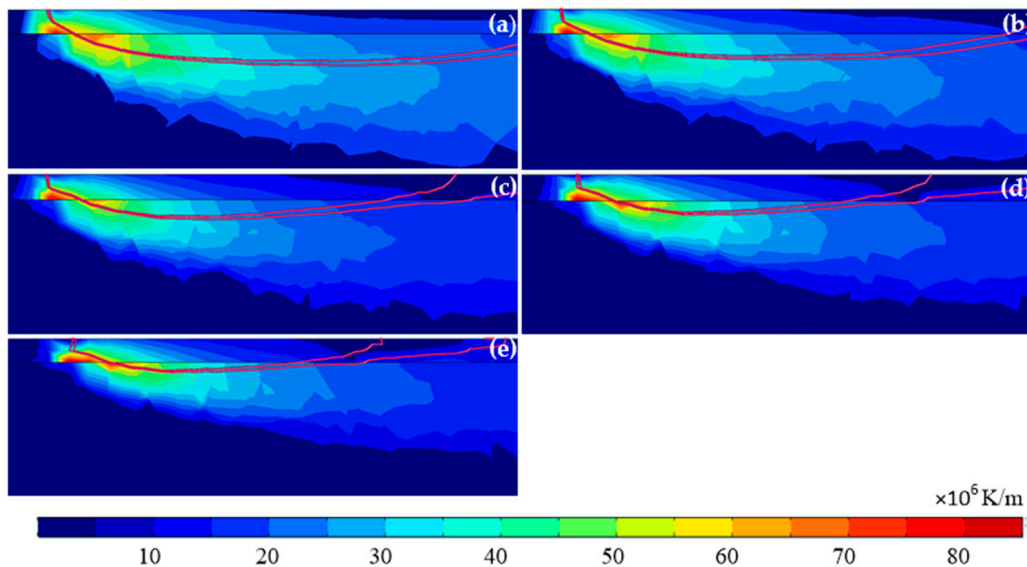


**Figure 6.** Effect of scanning speed on temperature gradient distribution, (a) 1000 mm/s, (b) 1100 mm/s, (c) 1200 mm/s, (d) 1400 mm/s, (e) 1600 mm/s.

The effect of the scanning speed on the temperature gradient and cooling rate in the molten pool is shown in Figure 7. The scanning speed affects both the temperature gradient and the cooling rate. When the scanning speed was increased from 1000 mm/s to 1600 mm/s, the temperature gradient was increased from  $5.64 \times 10^4$  K/cm to  $1.84 \times 10^5$  K/cm, and the cooling rate was increased from  $5.56 \times 10^5$  K/s to  $1.93 \times 10^6$  K/s. Through finite element simulation, scanning speed was noted to have a strong influence on both the temperature gradient and cooling rate in the range of molten pool. By introducing these data into the phase field model of the solidification process, the influence of the scanning speed on the micro-solidification structure can be simulated. This simulation constructed the bridge between the process parameters and the microstructure in both macro and micro scale.

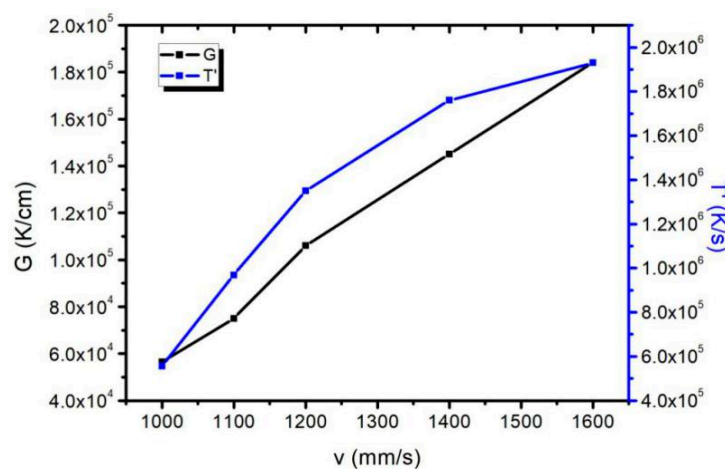


**Figure 7.** Effect of scanning speed on temperature gradient and cooling rate of molten pool.

### 3.2. Phase Field Simulation of Microstructures

The phase field distribution of different times at a scan speed of 1000 mm/s is shown in Figure 8. At  $t = 4$  ms, small crystal nuclei are formed on the plane and grow into dendritic arms along the direction of the temperature gradient. As the solidification time increases, competitive growth occurs between the small dendritic arms, and some of the dendrite arms continue to grow and eventually form a columnar structure. When the distance between the dendrite arms is large, the primary dendrite arm generates secondary dendrites perpendicular to the direction of the temperature gradient. Figure 9 presents a comparison of the simulated dendritic morphology with the actual dendritic morphology at a scanning speed of 1200 mm/s. It can be seen from the microstructure of the SLM sample that there is a columnar dendritic structure composed of columnar original  $\beta$  grains with grain boundaries. During the solidification of the Ti-6Al-4V alloy, the original  $\beta$  phase is formed from the liquid phase. The needle-like martensite phase ( $\alpha'$ ) will form if the untransformed  $\beta$  phase is subjected to temperatures below the martensite start temperature (923 K) [25]. The  $\beta$  phase does not have enough time to transform into the  $\alpha$  phase due to the rapid cooling of the molten pool, that gives rise to the formation of  $\alpha'$  phase, where the shape of the original  $\beta$  phase grain remains. The processes of the transition of Ti-6Al-4V alloy from the liquid to the solid phase, and the morphology of the original  $\beta$  phase are simulated by the phase field method. The simulated microstructures are similar to the Ti-6Al-4V samples processed by SLM.

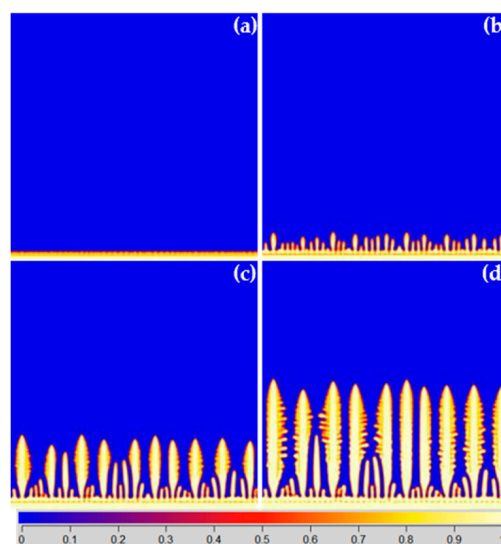


**Figure 8.** Phase field change with time, (a) 4 ms, (b) 8 ms, (c) 12 ms, and (d) 16 ms at  $v = 1000$  mm/s.

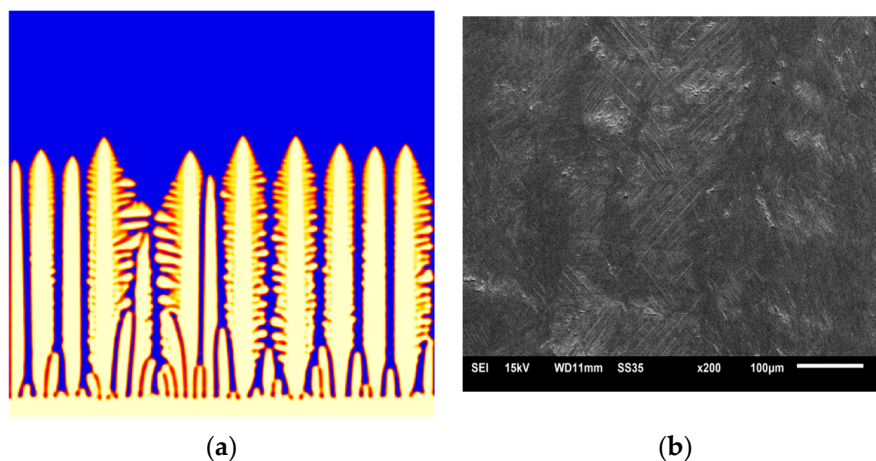


**Figure 9.** Dendritic morphology at a scanning speed of 1200 mm/s, (a) simulation result, (b) experimental results.



Figure 10 maps the distribution of the solute field at 1000 mm/s. The morphology of the concentration field distribution is similar to that of the phase field. At the beginning of solidification, the solutes enriched in the liquid phase near the tip of the dendrite arm. As the dendrite arm grows, the liquid phase concentration increases near the tip region and rapidly decreases to the alloy concentration away from the solidification front (the initial concentration is 10). In addition, the liquid phase concentration between the dendrite arms is higher than the dendrite tip.

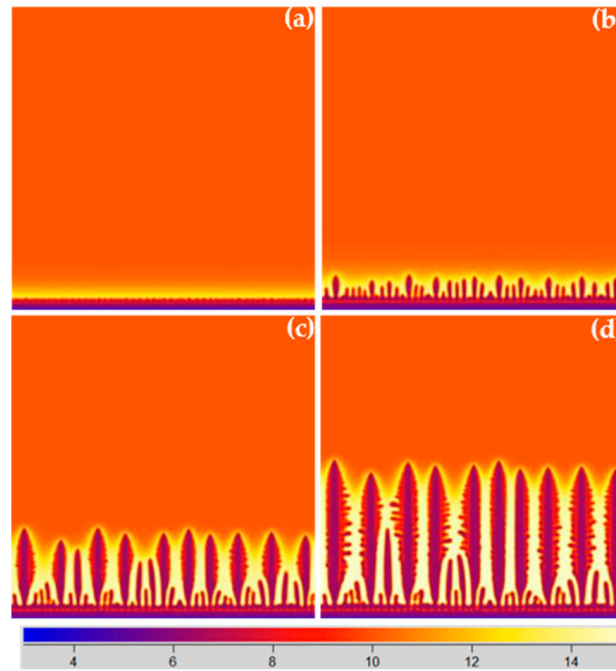


**Figure 10.** Solute field changes with time at  $v = 1000$  mm/s, (a) 4 ms, (b) 8 ms, (c) 12 ms, (d) 16 ms.

The microstructure evolution of Ti-6Al-4V alloy prepared by SLM was simulated by PF method with different scanning speeds, 1000 mm/s, 1100 mm/s, 1200 mm/s, 1400 mm/s, 1600 mm/s, as shown in Figure 11. From the phase field profile, the growth rate of the columnar crystals is slower at a scanning speed of 1000 mm/s. Due to the slower growth process, the spacing between the columnar dendrites is larger, and secondary dendrites are formed on the primary dendrites. As the scanning speed increases, the growth rate is bigger, the spacing between the columnar dendrites becomes smaller, and the secondary dendrites gradually disappear, for example at 1600 mm/s, the dendrites are finer. Figure 12 maps the columnar dendrite arm spacing and dendrite arm width, which vary with scanning speeds. It was also observed that the columnar dendrite arm spacing and the dendrite arm width decreased with increased scanning speed.

Hunt et al. [26] proposed a theoretical model for quantifying the dendrite spacing, predicting the dendrite arm spacing by considering the geometry of the dendrite tip, here expressed by PDAS (primary dendritic arm spacing), i.e.,

$$\text{PDAS} = 2.83(k\Gamma\Delta T_0 D_l)^{0.25} G^{-0.5} V^{-0.25} \quad (6)$$

where  $k$  is the partition coefficient,  $\Gamma$  is the Gibbs Thomson coefficient,  $\Delta T_0$  is the temperature change interval,  $D_l$  is the liquid phase diffusion coefficient,  $G$  is the temperature gradient, and  $V$  is the dendrite growth rate.

Kurz et al. [27] modified the model by considering the overall effect of the dendritic tip and branches:

$$\text{PDAS} = 4.3(k\Gamma\Delta T_0 D_l)^{0.25} G^{-0.5} V^{-0.25}. \quad (7)$$

The comparison between the simulated value and the classical model is shown in Figure 13. As the scanning speed increases, the overall distribution trend of the simulated values is similar to the classical model. When the scanning speed is lower than 1200 mm/s, the analog values are distributed between two model values, which are in good agreement with the classical model. When the scanning speed is greater than 1200 mm/s, the decreasing tendency of the analog value as the scanning speed increases is slowed down, where at 1600 mm/s, the simulated dendrite spacing is even bigger than the dendrite spacing at 1400 mm/s. Of course, in actual production, the scanning speed generally does not exceed 1600 mm/s.

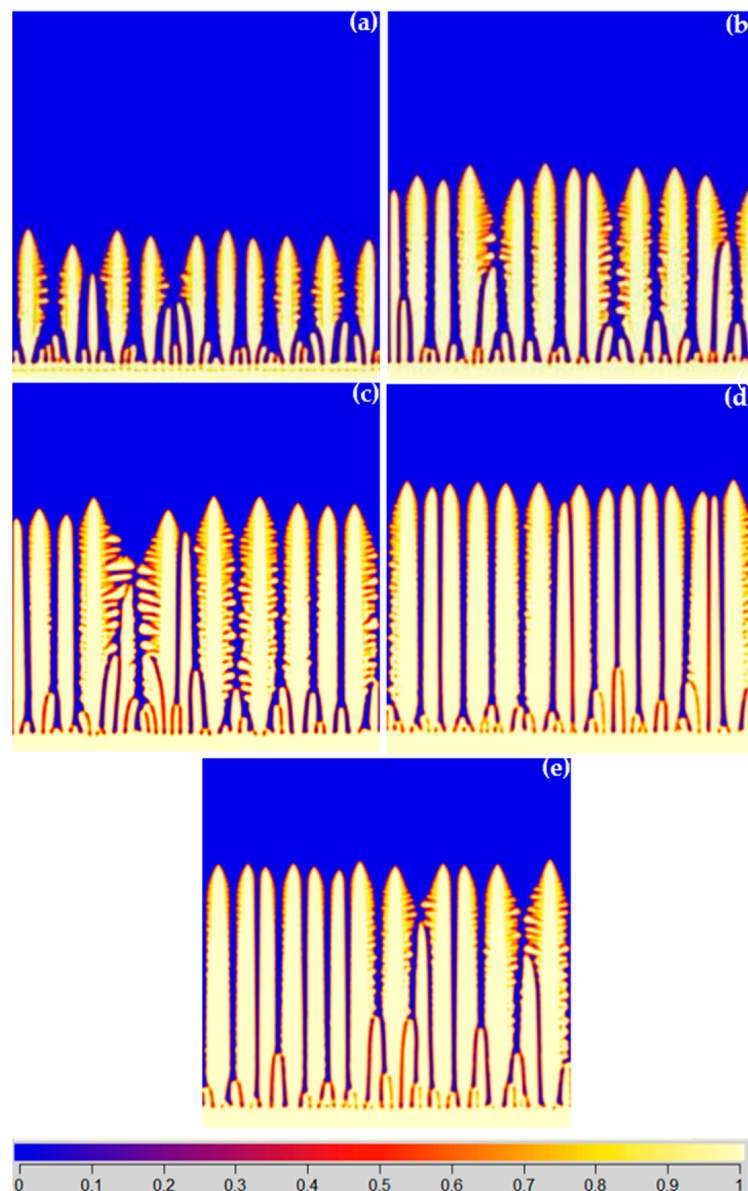


**Figure 11.** Influence of scanning speed on phase field distribution (a) 1000 mm/s, (b) 1100 mm/s, (c) 1200 mm/s, (d) 1400 mm/s, (e) 1600 mm/s).

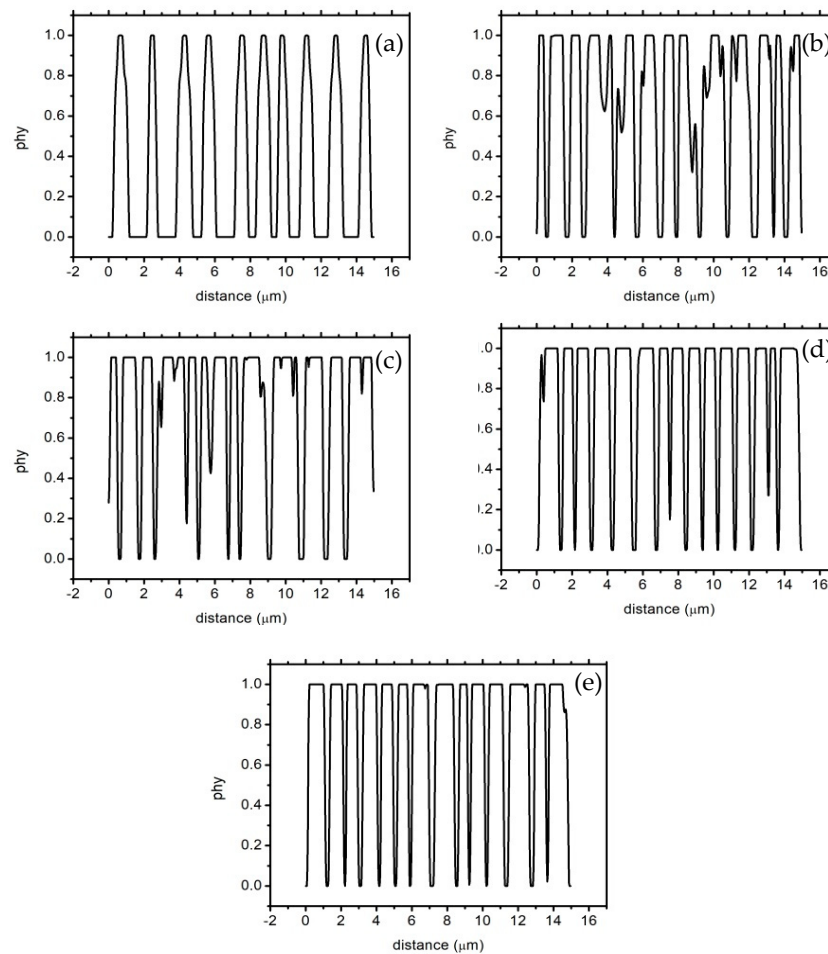


**Figure 12.** Effect of scanning speed on dendrite spacing, (a) 1000 mm/s, (b) 1100 mm/s, (c) 1200 mm/s, (d) 1400 mm/s, (e) 1600 mm/s.

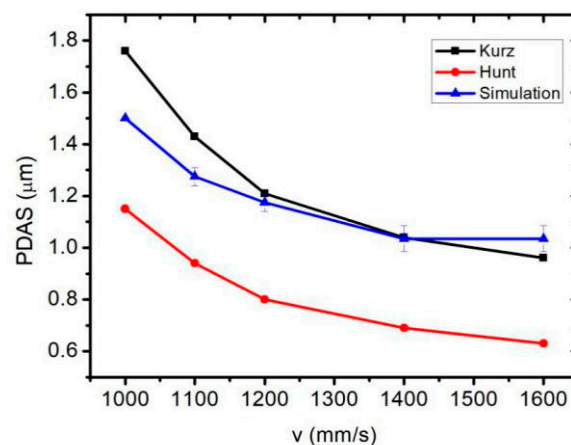


**Figure 13.** Comparison of simulation results with classical models.

#### 4. Conclusions

The study shows that combining the finite element model with the phase field model can obtain more accurate simulation results. The main conclusions are summarized as follows:

- (1) The finite element simulation can obtain the temperature field and temperature gradient distribution in the SLM process, and the two correspond to each other in the macroscopic range.

- (2) The scanning speed affects the temperature gradient and cooling rate within the bath. When the scanning speed was increased from 1000 mm/s to 1600 mm/s, the temperature gradient was increased from  $5.64 \times 10^4$  K/cm to  $1.84 \times 10^5$  K/cm, and the cooling rate was increased from  $5.56 \times 10^5$  K/s to  $1.93 \times 10^6$  K/s.
- (3) The phase field method can simulate the transition of Ti-6Al-4V from liquid phase to solid phase during solidification, and the microstructure morphology is columnar dendrite growing along the direction of temperature gradient.
- (4) Microscopic segregation was observed during the formation of dendrites, and it was found that the solute was concentrated in the liquid phase near the tip of the dendrite and between the dendrite arms.
- (5) Scanning speed has an effect on the pitch of the dendrite arm. By increasing the scanning speed from 1000 mm/s to 1600 mm/s, the distance between the main arms is reduced from 1.50  $\mu\text{m}$  to 1.07  $\mu\text{m}$ .

**Author Contributions:** Conceptualization, H.C.; Data curation, L.D.; Formal analysis, L.D.; Funding acquisition, H.C.; Investigation, F.L.; Methodology, G.X.; Software, L.D. and Z.L.; Supervision, Z.S.

**Funding:** This work was supported by Jiangsu Key R&D Program (BE2019119).

**Conflicts of Interest:** The authors declare no conflict of interest.

## References

1. Gibson, I.; Rosen, D.; Stucker, B. Development of additive manufacturing technology. In *Additive Manufacturing Technologies*; Springer: New York, NY, USA, 2015; pp. 19–42.
2. Guo, N.; Ming, C.L. Additive manufacturing: Technology, applications and research needs. *Front. Mech. Eng. Chin.* **2013**, *8*, 215–243. [[CrossRef](#)]
3. Lewandowski, J.J.; Seifi, M. Metal additive manufacturing: A review of mechanical properties. *Annu. Rev. Mater. Res.* **2016**, *46*, 151–186. [[CrossRef](#)]
4. Bourell, D.L. Perspectives on additive manufacturing. *Annu. Rev. Mater. Res.* **2016**, *46*, 1–18. [[CrossRef](#)]
5. Cruz, K.S.; Meza, E.S.; Fernandes, F.A.P.; Quaresma, J.M.V.; Casteletti, L.C.; Garcia, A. Dendritic arm spacing affecting mechanical properties and wear behavior of Al-Sn and Al-Si alloys directionally solidified under unsteady-state conditions. *Metall. Mater. Trans. A* **2010**, *41*, 972–984. [[CrossRef](#)]
6. Osorio, W.R.; Goulart, P.R.; Garcia, A.; Santos, G.A.; Neto, C.M. Effect of dendritic arm spacing on mechanical properties and corrosion resistance of Al 9 wt pct Si and Zn 27 wt pct Al alloys. *Metall. Mater. Trans. A* **2006**, *37*, 2525–2538. [[CrossRef](#)]
7. Razavi, S.M.-J.; Ferro, P.; Berto, F. Fatigue assessment of Ti-6Al-4V circular notched specimens produced by selective laser melting. *Metals* **2017**, *7*, 291. [[CrossRef](#)]
8. Zhang, P.; He, A.N.; Liu, F.; Zhang, K.; Jiang, J.; Zhang, D.Z. Evaluation of low cycle fatigue performance of selective laser melted titanium alloy Ti-6Al-4V. *Metals* **2019**, *9*, 1041. [[CrossRef](#)]
9. Rafi, H.K.; Karthik, N.V.; Gong, H.; Starr, T.L.; Stucker, B.E. Microstructures and mechanical properties of Ti6Al4V parts fabricated by selective laser melting and electron beam melting. *J. Mater. Eng. Perform.* **2013**, *22*, 3872–3883. [[CrossRef](#)]
10. Zhou, B.; Zhou, J.; Li, H.; Feng, L. A study of the microstructures and mechanical properties of Ti-6Al-4V fabricated by SLM under vacuum. *Mater. Sci. Eng., A* **2018**, *724*, 1–10. [[CrossRef](#)]
11. Popovich, A.; Sufiiarov, V.; Borisov, E.; Polozov, I.A. Microstructure and mechanical properties of Ti-6Al-4V manufactured by SLM. *Key Eng. Mater.* **2015**, *651*, 677–682. [[CrossRef](#)]
12. Thijs, L.; Verhaeghe, F.; Craeghs, T.; Humbeeck, J.V.; Kruth, J.P. A study of the microstructural evolution during selective laser melting of Ti-6Al-4V. *Acta Mater.* **2010**, *58*, 3303–3312. [[CrossRef](#)]
13. Roberts, I.A.; Wang, C.J.; Esterlein, R.; Stanford, M.; Mynors, D.J. A three-dimensional finite element analysis of the temperature field during laser melting of metal powders in additive layer manufacturing. *Int. J. Mach. Tools Manuf.* **2009**, *49*, 916–923. [[CrossRef](#)]
14. Yang, J.; Sun, S.; Brandt, M.; Yan, W. Experimental investigation and 3D finite element prediction of the heat affected zone during laser assisted machining of Ti-6Al-4V alloy. *J. Mater. Process. Technol.* **2010**, *210*, 2215–2222. [[CrossRef](#)]

15. Foroozmehr, A.; Badrossamay, M.; Foroozmehr, E.; Golabi, S.I. Finite element simulation of selective laser melting process considering optical penetration depth of laser in powder bed. *Mater. Des.* **2015**, *89*, 255–263. [[CrossRef](#)]
16. Zhuang, J.R.; Lee, Y.T.; Hsieh, W.H.; Yang, A.S. Determination of melt pool dimensions using doe-fem and rsm with process window during slm of Ti–6Al–4V powder. *Opt. Laser Technol.* **2018**, *103*, 59–76. [[CrossRef](#)]
17. Salsi, E.; Chiumenti, M.; Cervera, M. Modeling of microstructure evolution of Ti–6Al–4V for additive manufacturing. *Metals* **2018**, *8*, 633. [[CrossRef](#)]
18. Gong, X.; Chou, K. Phase-field modeling of microstructure evolution in electron beam additive manufacturing. *JOM* **2015**, *67*, 1176–1182. [[CrossRef](#)]
19. Sahoo, S.; Chou, K. Phase-field simulation of microstructure evolution of Ti–6Al–4V in electron beam additive manufacturing process. *Addit. Manuf.* **2016**, *9*, 14–24. [[CrossRef](#)]
20. Wu, L.; Jing, Z. Phase field simulation of dendritic solidification of Ti–6Al–4V during additive manufacturing process. *JOM* **2018**, *70*, 2392–2399. [[CrossRef](#)]
21. Consultants, C. *Comsol Multiphysics Version 4.3 Highlights*; COMSOL AB: Stockholm, Sweden, 2015.
22. Elmer, J.W.; Palmer, T.A.; Babu, S.S.; Zhang, W. Phase transformation dynamics during welding of Ti–6Al–4V. *J. Appl. Phys.* **2004**, *95*, 8327–8339. [[CrossRef](#)]
23. Nastac, L. “Cfd modeling and simulation in materials processing” symposium. *Metall. Mater. Trans. B* **2014**, *45*, 12. [[CrossRef](#)]
24. Ramirez, J.C.; Beckermann, C.; Karma, A.; Diepers, H.J. Phase-field modeling of binary alloy solidification with coupled heat and solute diffusion. *Phys. Rev. E: Stat. Nonlinear Soft Matter Phys.* **2004**, *69*, 051607. [[CrossRef](#)] [[PubMed](#)]
25. Echebarria, B.; Folch, R.; Karma, A.; Plapp, M. Quantitative phase-field model of alloy solidification. *Phys. Rev. E: Stat. Nonlinear Soft Matter Phys.* **2004**, *70*, 061604. [[CrossRef](#)] [[PubMed](#)]
26. Burden, M.H.; Hunt, J.D. Cellular and dendritic growth. I. *J. Cryst. Growth* **1974**, *22*, 109–116. [[CrossRef](#)]
27. Kurz, W.; Fisher, D.J. Dendrite growth at the limit of stability: Tip radius and spacing. *Acta Metall.* **1981**, *29*, 11–20. [[CrossRef](#)]



© 2019 by the authors. Licensee MDPI, Basel, Switzerland. This article is an open access article distributed under the terms and conditions of the Creative Commons Attribution (CC BY) license (<http://creativecommons.org/licenses/by/4.0/>).